

AeroMesa: Efficient Data Management System for Multi-Dimensional Spatio-Temporal Trajectories

Yue Zhang¹, Zizhong Ding¹, Lin Sun¹, Haopeng Chen^{1,*}, Yan Jiao², Yongming Xu²

¹ Shanghai Jiao Tong University, Shanghai, China

² ShangHai Shapere Information Technology Co.,Ltd., Shanghai, China

Email: {zhangyue20040611, enutrof65536, sun_lin, chen-hp}@sjtu.edu.cn; {jiao, xu}@shapere.xyz

Abstract—The rapid growth of trajectory data—especially the dense 4D traces generated by unmanned aerial vehicles (UAVs)—is placing mounting pressure on spatio-temporal data management systems. Existing HBase-based trajectory indexes suffer from three limitations: coarse-grained temporal pruning, locality-unfriendly XZ2 spatial encodings with workload-blind ordering, and severe row-key interval fragmentation when altitude is jointly encoded with the horizontal dimensions. We present *AeroMesa*, a unified system that natively supports (x, y) , (x, y, t) , (x, y, z) , and (x, y, z, t) queries within a single storage framework. *AeroMesa* integrates three complementary designs: a temporal index (TI⁺) that refines pruning to second-level granularity, a Hilbert-BFS spatial index with a Workload-Aware Jaccard ordering, and a decoupled 4D architecture that separates horizontal indexing from altitude-aware secondary indexing to eliminate isotropic-encoding fragmentation. We implement *AeroMesa* on Apache HBase and Redis and evaluate it on a real-world dataset (T-Drive) and a high-fidelity 90,000-trajectory UAV simulation dataset. *AeroMesa* consistently outperforms all baselines: TI⁺ cuts temporal-query candidates by up to 51% over MCTM, the Hilbert-BFS/WAJ index lowers 2D latency by up to 17.9% over the state-of-the-art TMan, and the decoupled 4D design reduces latency by up to 30× while cutting merged scan ranges by up to three orders of magnitude over XZ3/TXZ3 joint-encoding approaches.

Index Terms—spatio-temporal data, trajectory

I. INTRODUCTION

Trajectory data management has become a fundamental capability for intelligent transportation, logistics, and urban planning. Large-scale platforms continuously collect location traces from vehicles, couriers, and mobile sensing devices. For example, JD Logistics has reported that more than 60,000 couriers generate over 1TB of trajectory logs per day [1]. This trend is further intensified by the emerging low-altitude economy, where unmanned aerial vehicles (UAVs) are increasingly used for parcel delivery, infrastructure inspection, and emergency response. Compared with conventional ground trajectories, UAV traces introduce altitude as an extra dimension, driving trajectory repositories to jointly support (x, y) , (x, y, t) , (x, y, z) , and (x, y, z, t) queries within a single storage framework.

Distributed key-value stores, particularly Apache HBase, are an attractive substrate for this setting because they offer horizontal scalability, high write throughput, and a mature operational ecosystem. Representative systems such as TrajMesa [2], VRE [3], and TMan [4] have shown that HBase

can effectively support large-scale planar trajectory management. However, extending such systems from 2D workloads to unified multi-dimensional workloads is not as simple as lifting an existing 2D spatial encoding to a 3D or 4D one. A straightforward approach is to replace the 2D space-filling curve with a 3D one and jointly encode altitude with horizontal coordinates in a single spatial key space. In practice, this strategy is poorly matched to the anisotropic physical scales of trajectory dimensions: the horizontal domain usually spans large geographic regions, whereas UAV altitude is typically confined to a much narrower range. Once these dimensions are normalized into the same encoded space, practical query windows often become badly misaligned with the induced grid partitioning. In HBase, this misalignment manifests as a large number of disjoint row-key intervals, which increases RPC overhead and diminishes the benefit of sequential scans. Avoiding such row-key interval fragmentation while still supporting altitude predicates is therefore a primary challenge in HBase-based multi-dimensional trajectory management.

Beyond this architectural issue, the efficiency of existing spatial and temporal access paths is also limited. On the spatial side, TMan proposes a two-level approach: high-level XZ2 encodings for spatial cells and low-level geometric Jaccard reordering on intra-cell shape codes. Unfortunately, high-level XZ2 suffers from structural jumps inherent to Z-ordering which destroy physical locality. At the low level, geometric Jaccard reordering ignores the fact that, in skewed query workloads, specific shape-code patterns are frequently co-accessed. On the temporal side, existing coarse-grained time-slot encodings often lose precise intra-slot boundary information, causing false positives. Taken together, these observations suggest that a unified HBase-based trajectory management system must solve two problems simultaneously: **it must avoid row-key interval fragmentation at the architectural level, and it should improve spatial locality and pruning precision at the access-path level.**

To this end, we present *AeroMesa*, a unified multi-dimensional trajectory management system built on a decoupled architecture that avoids forcing a highly anisotropic domain into a single joint spatial encoding. *AeroMesa* utilizes a primary **Spatial Index (SI)** that encodes only xy (longitude-latitude) information, combined with a server-side **ZFilter** which pushes down altitude predicates, to continuously preserve horizontal locality while enabling efficient altitude prun-

ing for 3D queries. For 4D spatio-temporal queries, we introduce a secondary index table, called the **Height Spatial-Temporal Index (HTSI)**, which leverages multi-granularity altitude slots to prune away data except the queried altitude slot. This confines the scan to only the relevant altitude band rather than sweeping across all heights.

Within this decoupled architecture, AeroMesa further enhances the underlying access paths. To improve spatial locality, AeroMesa proposes a **Hilbert-BFS** encoding coupled with a **Workload-Aware Jaccard (WAJ)** reordering metric. Unlike purely geometric Jaccard, WAJ blends shape-code similarity with query-workload co-access frequency. For temporal precision, AeroMesa introduces **TI+**, an enhanced temporal index that tracks fine-grained intra-bucket boundaries. By supporting exact intra-bucket boundary checks at the key-value level, TI+ can reduce false positives in temporal range queries and lower overall query latency.

We implement AeroMesa on top of Apache HBase and Redis. Extensive evaluations are conducted using a large-scale trajectory dataset (T-Drive) and a high-fidelity UAV dataset, the latter containing approximately 90,000 simulated flights over a $10\text{ km} \times 10\text{ km}$ low-altitude airspace in Shanghai.

The main contributions of this paper are as follows:

- We design an efficient multi-dimensional spatio-temporal trajectory data management system. The system natively supports (x, y) , (x, y, t) , (x, y, z) , and (x, y, z, t) queries within a unified storage framework. By eliminating row-key interval fragmentation through a decoupled horizontal-altitude architecture, it reduces query latency by $10\times$ – $30\times$ over XZ3 and TXZ3 joint encodings for 3D and 4D workloads, with contiguous scan intervals reduced by up to three orders of magnitude. For 4D queries, HTSI further reduces latency by 21%–54% and cuts the candidate segment set by up to 76%.
- We propose a suite of novel indexing techniques. Hilbert-BFS encoding, coupled with Workload-Aware Jaccard reordering, improves planar spatial locality, reducing latency by 8.3%–17.9% over TMan and 84.4%–89.3% over GeoMesa on 2D queries. TI+ augments time-slot encoding with exact intra-bucket boundary checks, reducing candidate segments by up to 51.3% and average temporal query time by up to 21.2% over MCTM for short temporal windows.
- We implement AeroMesa on Apache HBase and Redis, demonstrating robust scalability across both read and write operations. Under a $200\times$ data-volume expansion, query latency increases by only $11.03\times$, confirming sub-linear read scalability. Meanwhile, amortized write costs scale gracefully, showing only a $4.3\times$ increase against a $1000\times$ growth in store size, proving its efficiency in handling large-scale, high-density trajectory data.

II. RELATED WORK

A. Trajectory Management Systems

Early single-machine systems such as TrajStore [5] and Torch [6] suffer from inherent scalability limits. Distributed

and in-memory systems—including ST-Hadoop [7], Summit [8], UITraMan [9], DITA [10], TrajSpark [11] and Dragon [12]—improve throughput and scale but remain uneconomical for large-scale historical trajectory storage or support only a limited query scope. Relational extensions such as MobilityDB [13] and spatial Spark frameworks such as Simba [14] and GeoSpark [15] offer complementary capabilities but are either limited in scalability or provide insufficient spatio-temporal support.

Modern NoSQL-based systems differ primarily in storage granularity. Point-based systems (e.g., GeoMesa [16]) support precise queries but suffer from severe write amplification. Trajectory-based systems (e.g., TrajMesa, TMan) avoid write amplification but must scan entire trajectories to answer range queries. Segment-based systems (e.g., VRE, MCTM [17]) offer a practical middle ground. On the indexing side, early systems such as TrajMesa and THBase [18] replicate data across multiple primary tables, incurring high storage costs; later systems such as TMan, VRE, and MCTM replace this with a single primary table plus lightweight secondary indexes.

However, no existing system provides unified support for (x, y) , (x, y, t) , (x, y, z) , and (x, y, z, t) queries within a single framework—a gap AeroMesa fills for UAV and low-altitude trajectory workloads.

B. Spatial Index

R-tree [19] and its variants [20], [21] are widely used for multi-dimensional indexing, but their dynamic rebalancing incurs significant write latency under high-throughput ingestion, making them unsuitable for large-scale HBase-backed systems [22]. Hilbert R-tree [23] and CSE-tree [24] improve clustering but retain dynamic tree structures with prohibitive maintenance overhead in write-intensive key-value stores.

Geohash encodes 2D coordinates via Z-order curves but does not extend to range-bearing objects such as trajectory segments. XZ-Ordering [25] addresses this with double-enlarged elements representing segment MBRs, and has been widely adopted by GeoMesa, TrajMesa, JUST [26], VRE, TraSS [27], MCTM, and TMan. Subsequent work refined the approach: TrajMesa introduced XZ2+ with PosCode, MCTM proposed an Index Cache, and TMan appends Jaccard-ordered shape codes to reduce scan intervals.

Hilbert curves offer better locality than Z-order curves [28] and have been studied for point data [29], but no prior work has proposed a Hilbert-based enlarged-element strategy for trajectory segments. For 3D indexing, naively extending XZ2 to XZ3 treats altitude as an equivalent spatial dimension, causing severe resolution imbalance for UAV trajectories whose vertical range is orders of magnitude smaller than their horizontal extent. AeroMesa instead encodes only horizontal coordinates via Hilbert-BFS and handles altitude filtering independently through HBase-side ZFilters.

C. Temporal Index

Interval trees and segment trees support exact interval matching but are ill-suited for key-value databases under

concurrent ingestion. Most trajectory systems therefore adopt a time-binning strategy. ST-Hadoop establishes this paradigm but produces false positives when query windows are narrower than a bin. TrajMesa’s XZT index introduces up to 1/2 temporal dead space per level; VRE indexes by start time bin, causing wide over-scans; TMan records start and end bins at coarse granularity, materializing all boundary-intersecting segments. MCTM improves upon these with a single intra-SegTime offset, but for short segments fully inside one slot, the unknown opposite boundary still introduces false positives.

D. Spatio-Temporal Index

TB-tree [30] bundles spatiotemporally adjacent segments for improved locality but scales poorly due to dynamic tree maintenance. 3D R-tree [31] treats time as a third spatial dimension, but bounding-box overlap grows substantially along the time axis for long-term data. JUST-Traj [32] partitions time into intervals with separate spatial indexes per period, but uneven grid-level distribution fragments queries into many discrete scan intervals. MCTM structures its TSI as $BinNum + SI + SegTimeID$, improving I/O efficiency on key-value stores.

None of these systems index the altitude dimension, and folding altitude into the spatial encoding via XZ3 introduces severe scale imbalance.

III. FRAMEWORK

Figure 1 illustrates the overall architecture of AeroMesa, which consists of three main modules: Data Ingestion & Preprocessing, Indexing & Storage, and Query Processing.

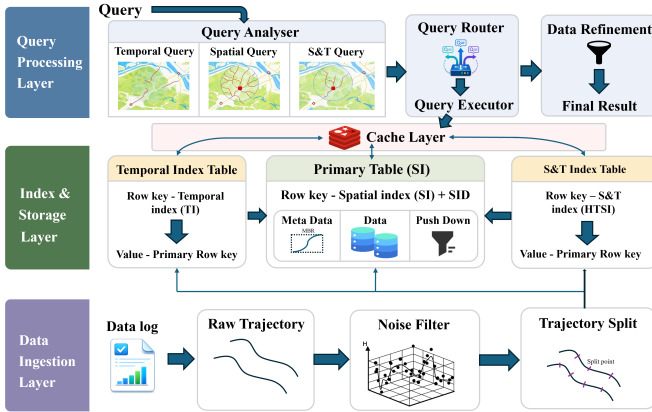


Fig. 1: The Framework of AeroMesa

Data Ingestion & Preprocessing. To achieve high-throughput trajectory data ingestion, this module implements a three-stage pipeline consisting of: 1) memory-mapped parsing, which utilizes Memory-Mapped I/O to map large files directly into off-heap memory, avoiding user-space data copying; 2) outlier filtering, which eliminates erroneous data points caused by signal instability; and 3) index-aligned segmentation, which dynamically partitions the continuous trajectory logs into atomic segments based on the pre-defined boundaries.

Indexing & Storage. To support diverse multi-dimensional queries within a unified system, AeroMesa adopts a primary-secondary table architecture. After segmentation, it organizes all data around a single primary storage table and persists the full system state across Apache HBase and Redis.

The primary table (SI table) uses a composite row key of the spatial index key and segment ID (SID). Each row stores the raw point sequence as a binary blob together with the trajectory MBR metadata, which serve as lightweight server-side attributes for pushdown pre-filtering. On top of this foundation, AeroMesa maintains three novel index structures.

The secondary index tables are backed by HBase by default, following the design of TMan. AeroMesa additionally provides a Redis-backed variant for both secondary indexes, allowing operators to trade storage cost for lower scan latency. Furthermore, AeroMesa maintains a per-cell shape-code set in Redis as a cache layer, enabling rapid in-memory shape-code pruning and substantially reducing false-positive candidates at negligible latency cost.

Query Processing. To efficiently support temporal, 2D/3D spatial, and 4D spatio-temporal queries, AEROMESA coordinates a three-stage processing pipeline. Each query is first parsed by a Query Analyser to identify its target dimensions, and then forwarded to a lightweight Query Router, which dispatches the query execution plan to the appropriate indexing layer for accelerated retrieval.

For *spatial queries*, the executor issues range scans directly against the primary SI table. Altitude predicates are pushed down to the HBase region server via a ZFilter, so mismatched segments are directly skipped before data leaves the server.

For *temporal queries* and *spatio-temporal queries*, the executor scans the secondary index for candidate IDs, then fetches payloads from the primary SI table with server-side filters (temporal boundary and ZFilter) applied.

Regardless of routing path, all queries conclude with a *refinement phase* that applies exact geometric verification on the retrieved payloads and returns the final results.

IV. INDEXING AND STORING

This section presents the indexing and storage design of AeroMesa. We begin with the trajectory data model that governs how raw point sequences are partitioned and stored (Section IV-A), then describe our storage schema built atop this model (Section IV-B). With the storage layout established, we introduce two index structures that accelerate query resolution: a two-level spatial index combining Hilbert-BFS macroscopic encoding with Workload-Aware Jaccard microscopic reordering (Section IV-C), and a temporal index TI^+ that eliminates false-positive fetches for short intra-interval trajectories (Section IV-D). We then extend this foundation to the anisotropic dimensional characteristics of 3D/4D trajectory data via a server-side ZFilter that prunes altitude-mismatched segments without joint encoding (Section IV-E) and the Height-Temporal-Spatial Index (Section IV-F).

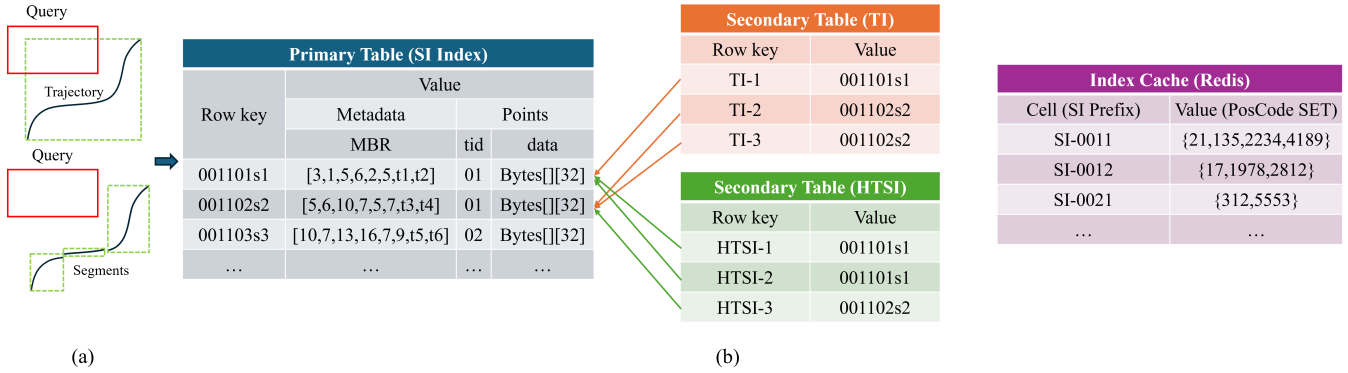


Fig. 2: Overview of AeroMesa’s three-tier storage schema: primary segment table, secondary index stores, and Index Cache.

A. Trajectory Model

A trajectory is generated by a moving object reporting its position at regular intervals. Each *trajectory point* is a tuple $p = \langle x, y, z, t \rangle$, where x and y denote horizontal coordinates, z denotes altitude, and t denotes the timestamp. A full trajectory $Traj$ is an ordered sequence of points $P = \{p_0, p_1, \dots, p_n\}$ sorted by timestamp.

Storing a full trajectory as a single row (trajectory-based model) produces large MBRs that poorly approximate the actual spatial extent, leading to false positives in range queries. Storing each point as an independent row (point-based model) incurs high write amplification and per-point indexing overhead. Following the segment-based paradigm of VRE and MCTM, as represented in Figure 2(a), AeroMesa partitions each trajectory into a sequence of non-overlapping segments.

AeroMesa uses fixed-duration time windows to partition trajectories: two consecutive points p_i and p_{i+1} are assigned to different segments when they cross a window boundary, formally defined as $[p_i.t / dur] \neq [p_{i+1}.t / dur]$, where dur is the fixed window duration. This yields a sequence of non-overlapping segments $Segs = \{seg_0, seg_1, \dots, seg_m\}$, each stored as a single HBase row.

B. Storage Schema

AeroMesa organises all persistent state across three tiers, as shown in Figure 2(b):

Primary Table: The primary table stores the segment data together with its multidimensional metadata. AeroMesa constructs the row key by concatenating three fields:

$$rowkey = \underbrace{partition_id}_{\text{configurable prefix}} \text{“-”} \underbrace{SI}_{\text{Spatial Index}} \text{“-”} \underbrace{sid}_{\text{segment id}} \quad (1)$$

The `partition_id` prefix controls the trade-off between locality and load balance and can be tuned per deployment, for example via equal-frequency quantiles of the rowkey distribution to ensure balanced region load in distributed settings. The packed spatial index SI (as detailed in Section IV-C) ensures

that spatially adjacent segments cluster within each partition. The segment identifier sid uniquely identifies each segment.

Each row stores two parts. The **metadata** column family holds the segment’s four-dimensional MBR, which are evaluated by server-side filters *before* the payload is read, enabling spatial, altitude, and temporal pruning without decoding raw points. The **payload** column family stores the serialised point list as a compact binary blob (32 bytes per point).

Secondary Tables: To support multiple query types without duplicating raw payloads, AeroMesa maintains lightweight secondary tables that map index keys (e.g., HTSI or TI+ codes) to the corresponding primary row keys. These tables can be backed by either Redis or a HBase table depending on deployment requirements.

Index Cache: Verifying all shape codes in a spatial cell against the query window on every query incurs unnecessary I/O overhead. AeroMesa addresses this by maintaining a Redis SET per spatial cell that records every distinct shape code ever written into that cell. At query time, a single set-membership lookup retrieves the populated codes; intersecting this set with the geometrically overlapping shape codes for the query window yields a small candidate list, each entry then resolved via a targeted score-range scan.

The cache is append-only by design: shape codes are never explicitly removed. A stale entry for a deleted segment introduces at most a false positive resolved at negligible cost by the downstream scan returning no matching rows, preserving correctness without requiring explicit invalidation.

C. Spatial Index

The storage schema above places segments into HBase rows ordered by a 1D key. The central challenge of spatial indexing is to assign 1D keys such that segments close in 2D space remain close on the key axis, minimising the number of disjoint HBase range scans required to answer a spatial query.

AeroMesa builds on the two-level spatial encoding paradigm of TMan’s TShape. In this paradigm, a *macroscopic* space-filling curve (SFC) maps each segment to a primary grid cell, while a *microscopic* 4×4 bitmask shape code

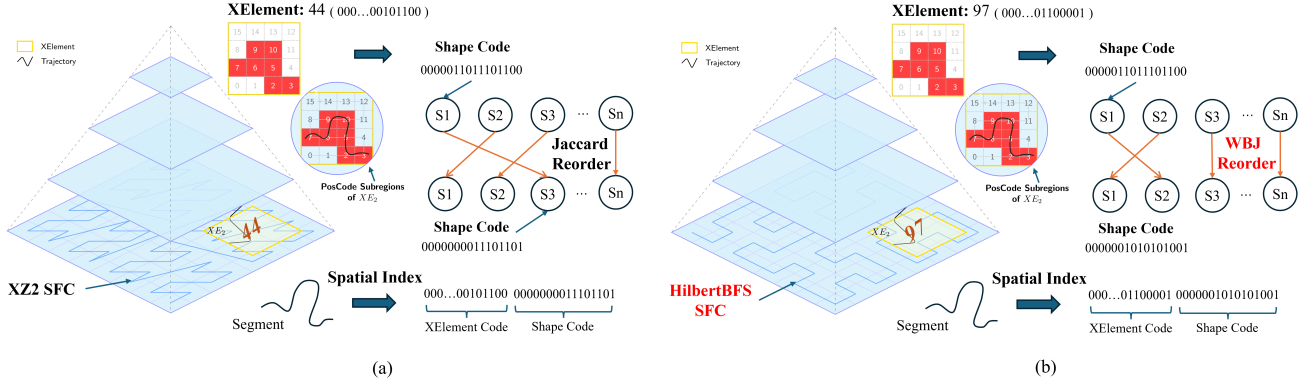


Fig. 3: Spatial index encoding pipeline: (a) TMan; (b) AeroMesa.

$s \in \{1, \dots, 2^{16} - 1\}$ captures the intra-cell footprint of the segment. TShape uses a Z-order SFC at the macroscopic level and a geometric Jaccard similarity shape-code reordering at the microscopic level (Figure 3(a)). Both choices carry known weaknesses: Z-order scatters spatially adjacent cells across discontinuous key intervals, and treating all sub-cell patterns equally wastes disk locality on rarely queried shapes. AeroMesa renovates both layers with **Hilbert-BFS** (where BFS denotes a breadth-first traversal of the quad-tree, ensuring that cells at the same resolution level remain contiguous in the encoding) and **Workload-Aware Jaccard (WJ)**, yielding the pipeline shown in Figure 3(b).

1) *Macroscopic Encoding: Hilbert-BFS:* AeroMesa retains the enlarged-cell construction and per-axis binary bisection of the TShape quad-tree, but replaces Z-order traversal with a 2D Hilbert-curve ordering. The Hilbert index of a segment is:

$$Index_{H-BFS}(seg) = \sum_{k=1}^{g-1} 4^k + \mathcal{H}_{2D}(C_i), \quad (2)$$

where $\mathcal{H}_{2D}(\cdot)$ is the standard 2D Hilbert index of the host cell C_i , and g is the depth at which the enlarged cell $E(C_i)$ first contains $MBR(seg)$, found by a BFS over the quad-tree. The offset $\sum_{k=1}^{g-1} 4^k$ ensures that cells at different depths map to disjoint key ranges, preserving injectivity across levels. A correct BFS termination requires that every MBR has a well-defined host cell; this is guaranteed by the enlargement strategy: at level l with cell side length δ_l , the base cell is extended by $2\delta_l$ in the positive x and y directions, so any MBR whose width and height are both smaller than δ_l is guaranteed to fall within the enlarged cell. Ties among siblings are broken deterministically by minimum Hilbert index.

a) *Why Hilbert outperforms Z-order.:* The benefit of the Hilbert curve is a reduction in the number of disjoint HBase scan calls required to cover a query window. Moon et al. prove the asymptotic expectations for a $2^k \times 2^k$ query region:

$$\mathbb{E}[\#\text{clusters}_{Hilbert}] \sim \frac{2^k}{3}, \quad \mathbb{E}[\#\text{clusters}_Z] \sim \frac{2^k}{2}, \quad (3)$$

as $k \rightarrow \infty$ – a 33% asymptotic reduction in scan fragments.

Empirical confirmation. On the T-Drive [33], holding shape code bits constant to isolate the macroscopic layer, Hilbert-BFS reduces HBase scan intervals by 40% versus XZ2.

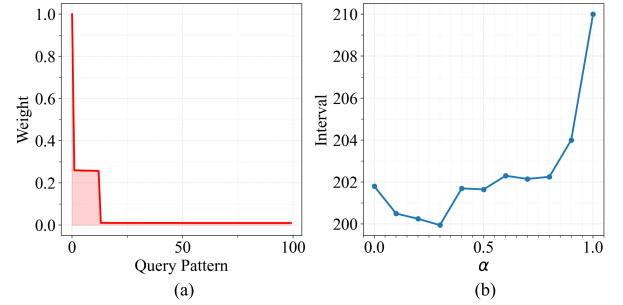


Fig. 4: WAJ workload analysis: (a) estimated pattern weight $\hat{P}(k)$; (b) α ablation (square workload).

2) *Microscopic Reordering: Workload-Aware Jaccard (WJ):* The Hilbert-BFS encoding determines which HBase cell a segment falls into; within that cell, the shape code determines which *sub-range* of the cell is scanned. TMan’s original ordering relies on geometric Jaccard similarity, treating all query patterns as equally likely. In practice, however, query workloads are skewed: a handful of boundary-crossing query patterns dominate query frequency. An ordering blind to this skew fails to cluster frequently co-accessed patterns into contiguous sub-ranges, fragmenting scans across scattered regions. AeroMesa addresses this with Workload-Aware Jaccard, which reorders shape codes according to observed query pattern frequency, in three steps.

a) *Step 1: bounding the achievable pattern space.:* Any axis-aligned query window Q intersects a cell in a *contiguous rectangular block* $[r_1, r_2] \times [c_1, c_2]$ of sub-cells. Since a 4×4 grid has 5 possible split positions per axis, the set \mathcal{K} of patterns that can actually be activated by a query satisfies:

$$|\mathcal{K}| \leq \binom{5}{2} = 100, \quad (4)$$

a $655 \times$ reduction from the naïve 2^{16} upper bound, so the prior need only be estimated over 100 patterns rather than 2^{16} .

b) *Step 2: estimating the query pattern frequency.*

For each achievable query pattern $k \in \mathcal{K}$, let $P(k)$ be the probability that a random boundary-intersecting cell exhibits pattern k under the observed workload. We estimate $P(k)$ via offline Monte Carlo sampling over $N = 100,000$ i.i.d. queries:

$$\hat{P}(k) = \frac{\text{boundary cells exhibiting pattern } k}{\text{total boundary cells across all queries}}. \quad (5)$$

By the Multivariate CLT, $\hat{P}(k)$ converges to $P(k)$ at rate $O(n^{-1/2})$, so $N = 100,000$ samples yield stable estimates. The resulting distribution is heavily skewed (Figure 4(a)): fewer than 12 of the 100 achievable patterns carry substantial weight, confirming the co-access concentration that a workload-aware ordering can exploit.

WAJ is robust to workload drift: $\hat{P}(k)$ depends only on *how* a query window crosses a cell, not on window center or absolute size, guaranteeing invariance to query-center and size drift by construction. Aspect-ratio drift has a mild effect on the chosen ordering (validated in Step 3), so a single offline estimate under a square workload suffices for deployment.

c) *Step 3: the WAJ similarity metric.*: Given $\hat{P}(k)$, the **CoHit** score measures how often two shape codes A and B are simultaneously activated by the same query pattern, where $A \& k \neq 0$ indicates that shape code A is activated by query pattern k (i.e., their bitmasks share at least one sub-cell):

$$\text{CoHit}(A, B) = \sum_{k \in \mathcal{K}} \hat{P}(k) \cdot \mathbf{1}[A \& k \neq 0] \cdot \mathbf{1}[B \& k \neq 0]. \quad (6)$$

The final WAJ similarity combines CoHit with the geometric Jaccard from TShape to preserve coarse spatial structure:

$$\text{WAJ}(A, B) = \alpha \cdot \widetilde{\text{CoHit}}(A, B) + (1 - \alpha) \cdot \widetilde{\text{Jacc}}(A, B), \quad (7)$$

where $\widetilde{\cdot}$ denotes min-max normalisation over all observed pairs. The mixing weight $\alpha = 0.30$ is selected by ablation over $\alpha \in \{0.1, 0.2, \dots, 0.9\}$: the interval count is minimized near $\alpha \approx 0.30$ and stays flat over $\alpha \in [0.2, 0.5]$ (Figure 4(b)), so the result is insensitive to the exact weight.

d) *Robustness to aspect-ratio drift.*: We stress-test the only drift axis on which $\hat{P}(k)$ has a non-trivial dependence. All curves in Figure 5 use a single weight vector $\hat{P}(k)$ estimated under the ratio-1 (square) workload and evaluated on progressively more elongated ones (up to 10:1 aspect ratio). Figure 5 thus functions as a cross-distribution generalisation test: across the entire range, the optimal α remains near 0.30 and the interval count stays flat, confirming that a square-workload estimate transfers without re-tuning even when the deployed query shape diverges substantially. This empirically validates the aspect-ratio robustness anticipated in Step 2, complementing the exact invariance to query-center and size scaling established there. Together, the three invariance results imply that a single offline-estimated $\hat{P}(k)$ remains valid across the full space of workload shifts—center, scale, and aspect ratio—so no re-tuning is required when the deployed query distribution diverges from the training workload.

Shape codes are then linearised by solving a maximum-weight Hamiltonian path on the WAJ similarity graph, since a

linear code ordering corresponds to a path visiting each node; following TMan, we approximate this NP-hard problem with a genetic algorithm. The resulting ordering is computed once at write time, remaining transparent to the query path.

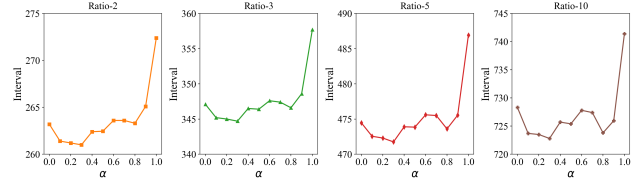


Fig. 5: WAJ cross-distribution robustness

3) *Update.*: On the update path, we introduce a flat main+delta LSM structure. Incoming segments are appended only to a lightweight delta index, avoiding per-write global WAJ re-encoding of the main index. Once the delta reaches a configurable threshold, a background compaction merges it into the main index in batch while queries continue to access the current version, guaranteeing read/write consistency throughout. This design decouples the expensive global re-ordering from the synchronous write path, reducing amortized write latency.

D. Temporal Index: TI^+

The spatial index improves locality to minimise disjoint range scans; the temporal index then prunes candidates that fall outside the query range. AeroMesa inherits the base temporal index structure from MCTM, which partitions the timeline into day bins and hourly intervals, assigning each segment a 32-bit packed index encoding day-bin, hourly-interval number, segment type, and a 9-bit intra-interval offset (≈ 7 s). MCTM defines three segment types: *type 2* (segment starts within this interval), *type 1* (segment spans the entire interval), and *type 0* (segment terminates within this interval).

a) TI^+ : *dual-offset type 3.*: A segment whose start and end both fall within the *same* hour interval is classified by MCTM as type 2, discarding the end-time information. At query time, the system cannot determine whether such a segment overlaps $[t_s, t_e]$ without fetching its raw points from HBase – incurring unnecessary I/O for segments that end before t_s or start after t_e .

AeroMesa introduces **type 3** for this case, as illustrated in Figure 6. When a segment is entirely contained within one hour interval, it is assigned *type = 3* and its index entry encodes a second 9-bit **end offset** alongside the start offset:

$$TI^+ = \underbrace{\underbrace{\text{BinNum}}_{\text{Day Bin: 16bits}} \parallel \underbrace{\text{SegTimeID}}_{\text{hour: 5bits}} \parallel \underbrace{\text{SegType}}_{\text{type: 2bits}} \parallel \underbrace{\text{Off}_9}_{9\text{bits}_s}}_{\text{original MCTM-TI: 32bits}} \parallel \underbrace{\text{Off}_9}_{9\text{bits}}$$

Both offsets use 9-bit binary-partition encoding with ≈ 7 s resolution, bounding the true time from both sides, enabling intra-hour overlap pruning directly from the index key.

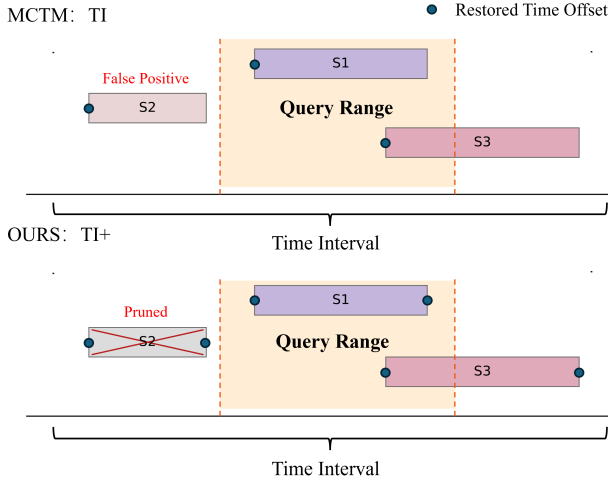


Fig. 6: TI^+ : type-3 entry for intra-hour boundary pruning.

E. 3D Extension: Altitude Filtering via ZFilter

The spatial and temporal indexes above operate in (x, y, t) . In the UAV domain, altitude is an extra query dimension: flight corridors are vertically separated by only tens of metres, yet span several kilometres horizontally—an extreme anisotropy that renders any naive isotropic 3D space-filling curve (e.g., XZ3 or Z3) ineffective for the low-altitude logistics domain.

a) *The aspect-ratio problem.*: Standard 3D indexes map the physical domain to the unit cube $[0, 1]^3$ via isotropic normalisation, implicitly assuming that all dimensions have comparable extents. In the UAV setting, however, the horizontal domain spans global scales ($L_{xy} \approx 40,000$ km) while the navigable vertical airspace is tightly bounded ($L_z \approx 1$ km), yielding a disparity of $L_{xy}/L_z \approx 4 \times 10^4$.

Isotropic normalisation therefore artificially stretches the Z -dimension, as shown in Figure 8. A query with physical footprint $5 \text{ km} \times 100 \text{ m}$ (aspect ratio 50:1) becomes a query with normalised extent ratio $\Delta q_z/\Delta q_{xy} = 800 : 1$. This distortion creates a dilemma with no satisfactory resolution within the isotropic framework:

- *Narrow z -range normalisation*: the Z coordinate aligns with physical reality, but a 100 m altitude query covers only $\sim 10^{-1}$ of the normalised Z axis, forcing the SFC to emit thousands of disjoint range intervals for even a thin horizontal slab (*index-range fragmentation*).
- *Wide z -range normalisation*: fragmentation is alleviated, but the same 100 m altitude band maps to a negligible fraction of the normalised axis, making the index insensitive to vertical predicates and reducing it to a 2D index.

This tension is not an artifact of a particular SFC choice; it is an intrinsic consequence of forcing a highly anisotropic domain into any single joint spatial encoding.

b) *Design response: decouple altitude from the SFC.*: Rather than searching for an optimal normalisation, AeroMesa removes altitude from the space-filling curve and keeps the primary ordering in (x, y, t) . Horizontal coordinates (x, y) are

handled by Hilbert-BFS (Section IV-C), while altitude is filtered by a dedicated **ZFilter** at the HBase RegionServer: since each segment row already stores $[z_{\min}, z_{\max}]$ in the `meta` column family (Section IV-B), altitude-mismatched segments are pruned *before* payload transfer, preserving horizontal index compactness and continuity.

This design is sufficient for 3D queries because the primary SI already provides spatial selectivity: a spatial range scan yields a compact candidate set, and ZFilter eliminates altitude mismatches within that set entirely server-side, incurring no additional RPC round-trips. Introducing a dedicated height-spatial secondary index would instead route candidates through rowkey-based Gets, whose per-entry RPC overhead outweighs the pruning benefit when the primary scan is already spatially selective. The case for a secondary altitude index arises when temporal locality is absent from the primary key: since the primary SI encodes spatial coordinates only, a 4D query over historical data degenerates into a full-history spatial scan, yielding a candidate set that grows unboundedly with data volume and cannot be tamed by ZFilter alone—precisely the condition that motivates HTSI for 4D queries (Section IV-F).

F. 4D Extension: Height-Temporal-Spatial Index (HTSI)

For 4D queries, AeroMesa augments the 3D path with a secondary index, the **Height-Temporal-Spatial Index** (HTSI), for altitude-aware candidate generation, as illustrated in Figure 7. HTSI and ZFilter operate in tandem: HTSI first constrains the candidate set to altitude-slot-aligned entries via a secondary index scan; ZFilter then eliminates residual false positives by checking exact $[z_{\min}, z_{\max}]$ metadata before any payload is transferred. In this secondary access path, end-to-end performance is highly sensitive to candidate precision and scan fan-out—both governed by where altitude is placed in the index key. This raises a central design question: should altitude live in the primary SI key, or in a dedicated secondary index?

a) *Why a secondary index rather than primary-key slotting.*: Embedding height-slot prefixes directly in the primary SI key is, in principle, feasible and may yield modest gains for narrow-band 3D queries by reducing RegionServer-side metadata predicate evaluation. However, this design is unfavourable for mixed workloads that combine frequent 2D access with large-altitude-range 3D queries. For 2D access (equivalently, full-height access), slot prefixes provide no pruning benefit yet fragment each scan range into $\lceil H/\Delta h \rceil = 2^{b_z}$ disjoint sub-ranges, where $b_z = \log_2(H/\Delta h)$ is the altitude bit depth. This $O(2^{b_z})$ penalty is fundamental to *all* joint altitude-encoding strategies: any asymmetric SFC with (a, a, c) bit allocation per axis achieves altitude cell width $\Delta_z = H/2^{c \cdot d}$ after d levels, so a full-height query still incurs $2^{c \cdot d}$ altitude cells—identical in form to the primary-key slotting case. Adaptive normalisation faces the same trade-off: any reduction in Δ_z that sharpens narrow-band selectivity amplifies wide-band fragmentation by the same factor. The tension is therefore intrinsic to joint encoding, not to any particular bit-allocation strategy. Maintaining a second, non-slotted primary layout to

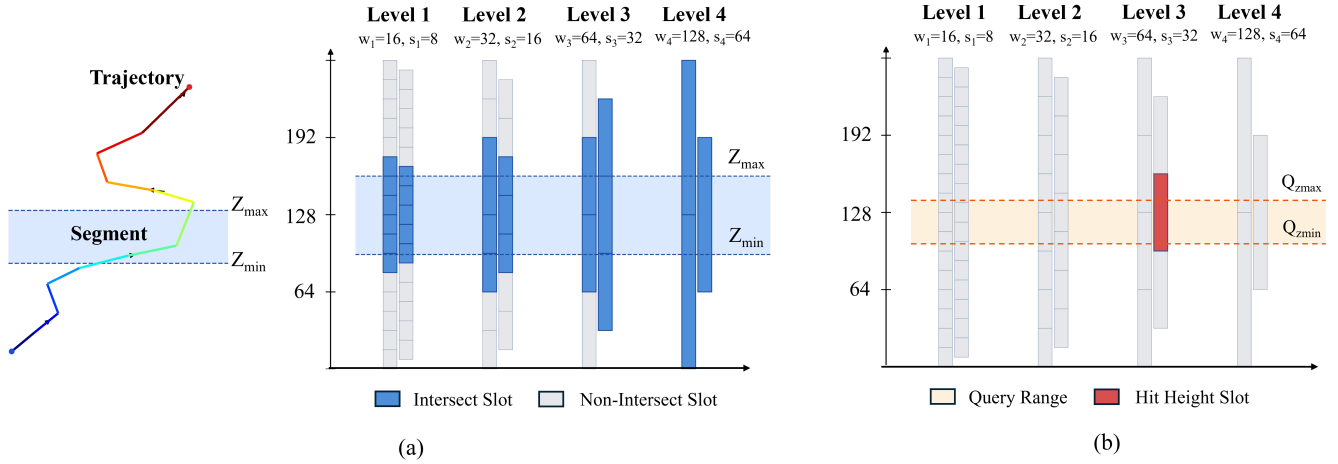


Fig. 7: Multi-granularity HeightSlot: (a) slot activation; (b) query-time selection.

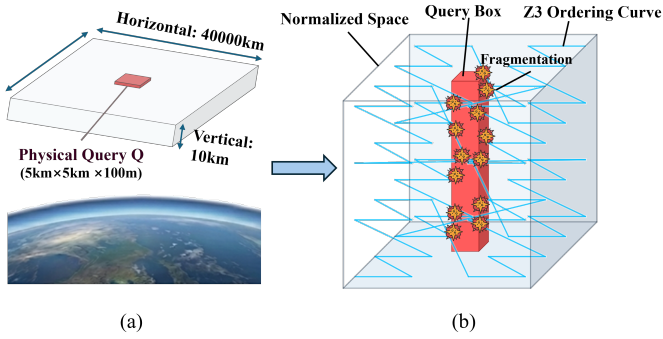


Fig. 8: Geometric distortion from isotropic indexing under aspect-ratio mismatch.

preserve 2D efficiency would require dual writes, doubling write amplification—unacceptable for our update path.

AeroMesa therefore keeps a *unified* primary SI for 2D/3D management and confines height-aware acceleration to HTSI. As a secondary index, HTSI sidesteps the $O(2^{b_z})$ penalty entirely: for altitude-bounded queries, the multi-granularity overlapping slot design—detailed in Section IV-F2—guarantees that any qualifying query resolves to a *single* contiguous HeightSlot scan (fan-out = 1). Because HTSI stores only lightweight index-to-rowkey mappings, the write amplification introduced by its multi-granularity HeightSlot prefixes is acceptable. Placing HeightSlot as the leading key component after the day bin constrains altitude-bounded queries to contiguous, altitude-aligned key ranges, reducing scan fragmentation and unnecessary downstream Gets—without the joint-encoding distortion that afflicts any joint-encoding strategy.

1) *Row Key Layout*: The core idea of HTSI is to exploit HBase’s byte-lexicographic ordering: by inserting a *HeightSlot* field between the day-level bin and the spatial-temporal score, all index entries sharing the same day and altitude slot become contiguous on disk. An HTSI row key is a composite

consisting of three distinct components:

$$\underbrace{BinNum}_{16 \text{ bits}} \mid \underbrace{HeightSlot}_{9 \text{ bits}} \mid \underbrace{LocalScore}_{8 \text{ Byte}} \quad (8)$$

where $BinNum = \lfloor t_{unix}/86400 \rfloor$ is the same day bin used by the base temporal index, and $LocalScore$ packs the spatial index and fine-grained temporal fields:

$$LocalScore = (SI \ll 5) \mid SegTimeID \quad (9)$$

where \ll denotes a left bit-shift; SI is the spatial index score (Section IV-C) and $SegTimeID \in [0, 23]$ is the hourly slot encoded in 5 bits. This ordering reflects a coarse-to-fine selectivity cascade: $BinNum$ partitions the key space at day granularity first, concentrating the scan within a bounded temporal window; $HeightSlot$ then sub-partitions within that window by altitude, yielding contiguous, doubly-constrained key ranges with minimal scan fan-out.

2) *Multi-Granularity Height Slot Design*: A single fixed altitude bucket size would be either too coarse (merging corridors that queries need to distinguish) or too fine (fragmenting the key space and inflating write amplification). HTSI instead employs *four granularity levels* with window widths $w = (16, 32, 64, 128)$ m. The range balances write amplification against altitude granularity: finer slots improve selectivity but multiply index entries per segment, while coarser slots reduce amplification at the cost of altitude discrimination.

Within each level k , the altitude domain $[0, 1024)$ m [34] is partitioned into overlapping windows of width w_k with a 50% stride:

$$\{[s_{k,i}, s_{k,i} + w_k)\}_{i \geq 0}, \quad s_{k,i} = i \cdot \frac{w_k}{2}. \quad (10)$$

This yields 127, 63, 31, and 15 slots for levels 1–4 respectively (236 total, encoded in 9 bits with $2^9 = 512 > 236$). The 50% overlap guarantees that any altitude range of span $\Delta z \leq w_k/2$ is fully covered by one level- k window, eliminating cross-slot boundary splits for sub-granularity queries. This stride is

the unique maximum preserving the guarantee: a larger stride would introduce uncovered gaps between adjacent windows, while a smaller stride increases write amplification without any improvement in coverage.

As shown in Figure 7(a), a segment spanning $[Z_{\min}, Z_{\max}]$ is indexed into every slot that intersects its altitude range across all four granularity levels. Segments with altitude outside the nominal domain are indexed only in the base TSI (the spatio-temporal index without HeightSlot prefixing), bypassing HTSI entirely.

a) *Query-time granularity selection.*: Given a query altitude range $[q_z^-, q_z^+]$ with span $\Delta q_z = q_z^+ - q_z^-$, the query engine selects the finest level k such that $\Delta q_z \leq w_k/2$, ensuring the query resolves to a single contiguous HeightSlot scan, as depicted in Figure 7(b). When $\Delta q_z > 64$ m—exceeding the half-window of the coarsest level ($w_4/2 = 64$ m)—no single HTSI level can guarantee single-slot coverage, and the query falls back to the base TSI. Queries with altitude bounds outside $[0, 1024]$ m are treated as anomalous and fall back likewise.

Since UAV operations follow altitude-stratified flight corridors governed by regulatory frameworks [34]–[36], the multi-granularity HeightSlot layout naturally aligns with physical flight corridors, distributing index entries across altitude levels and reducing hot-spotting within any single granularity tier.

3) *Write Amplification Analysis*: HTSI incurs $\approx 16\%$ write amplification relative to the primary table (vs. $\approx 1.2\%$ for the base TSI), as measured on our UAV dataset (Section VI-2). This overhead is acceptable because HTSI is a secondary index that stores only mappings to primary-table row keys, keeping each entry lightweight.

V. QUERY PROCESSING

AeroMesa supports three query types over the indexes introduced in Section IV: temporal query, spatial query, and spatio-temporal query. Queries translate to a few contiguous scans: temporal query and spatio-temporal query first scan their secondary tables to obtain candidate rowkeys, then get the matching rows from the primary table; spatial query scans the primary table directly. In both paths, independent scan ranges are issued to HBase concurrently using a fixed-size thread pool, hiding per-range round-trip latency. Predicate evaluation is pushed down to the HBase region server via server-side filters (MBR overlap, ZFilter, and temporal bound checks), so non-qualifying rows are discarded before network transfer.

A. Temporal Range Query

A temporal range query $q = [t_{qs}, t_{qe}]$ is answered by the TI+ index of Section IV-D. Let

$$\begin{cases} \text{Bin}_s = \lfloor t_{qs}/B \rfloor, \\ \text{Bin}_e = \lfloor t_{qe}/B \rfloor, \\ \text{Seg}_s = \lfloor (t_{qs} \bmod B)/\text{SegLen} \rfloor, \\ \text{Seg}_e = \lfloor (t_{qe} \bmod B)/\text{SegLen} \rfloor \end{cases} \quad (11)$$

with $B = 86400$ s and $\text{SegLen} = 3600$ s, TS_{qs} and TS_{qe} denote the 9-bit intra-segment offsets of t_{qs} and t_{qe} . Following the segment-type discipline of MCTM, type-0 (end) segments

in interval $_{qs}$ that finish before t_{qs} and type-2 (begin) segments in interval $_{qe}$ that start after t_{qe} must be excluded. Because the TI+ rowkey orders type $0 < 1 < 2 < 3$ within each hour, AeroMesa compiles the query into two contiguous index range scans that maximise sequential I/O while minimising candidate amplification:

$$R_A = [\text{Bin}_s \parallel \text{Seg}_s \parallel \text{type}0 \parallel \text{TS}_{qs}, \\ \text{Bin}_e \parallel \text{Seg}_e \parallel \text{type}2 \parallel \text{TS}_{qe}], \quad (12)$$

$$R_B = [\text{Bin}_e \parallel \text{Seg}_e \parallel \text{type}3 \parallel 0, \\ \text{Bin}_e \parallel \text{Seg}_e \parallel \text{type}3 \parallel \text{TS}_{qe}]. \quad (13)$$

R_A inherits the MCTM lower/upper sentinels and, by construction, admits zero type-0/1/2 false positives; R_B is a short auxiliary scan that captures the single-slice (type 3) entries which R_A would otherwise miss in the tail hour, while still guaranteeing $\text{startOffset} \leq \text{TS}_{qe}$. The middle hours $\text{Bin}_s : \text{Seg}_s + 1$ through $\text{Bin}_e : \text{Seg}_e - 1$ are fully contained inside the query window, so all of their entries (including type 3) are admitted by R_A without further filtering.

Only the type-3 entries in the boundary hour ($\text{Bin}_s, \text{Seg}_s$) (carried by R_A) and, in the single-hour case, by R_B may end before t_{qs} ; these are validated by the dual-offset filter,

$$\tau_{lo}(\text{startOffset}) \leq \text{TS}_{qe} \wedge \tau_{hi}(\text{endOffset}) \geq \text{TS}_{qs}, \quad (14)$$

using solely the offset values encoded in the retrieved boundary secondary index entries, and this check is performed before any access to the HBase payload table. Consequently, single-slice false positives never incur a payload read.

B. Spatial Range Query

Given a 2D box $Q_R = [x_l, x_h] \times [y_l, y_h]$, the generation of spatial query windows proceeds in three stages:

a) *Host-cell screening.*: The BFS walker descends \mathcal{T}_G and collects cells whose enlarged region overlaps Q_R . Cells fully covered by Q_R are explicitly marked and admitted directly without descending further, whereas partially overlapping cells are expanded to their children until the maximum depth is reached.

b) *Cache-pruned shape code resolution.*: Shape code filtering is *only* applied to partially overlapping cells. For each such cell C with masked address c , we retrieve the set $\mathcal{P}(c)$ of occupied shape codes from the Index Cache (Section IV-B) and compute the valid overlapping subset:

$$\mathcal{V}(c, Q_R) = \{ p \in \mathcal{P}(c) \mid p \& \text{ShapeCode}(Q_R \cap C) \neq 0 \}, \quad (15)$$

where $\text{ShapeCode}(\cdot)$ is the bitmap representation of the $\beta \times \beta$ sub-grid intersection.

c) *Window assembly.*: Each valid (c, p) pair from partially overlapping cells, as well as the inferred full-cell scan bounds from fully covered cells, produces narrow scan ranges over the Hilbert-BFS-WAJ-linearized local score. Two ranges are considered contiguous and merged if their endpoints differ by at most one (e.g., $[1, 5]$ and $[6, 9]$ merge into $[1, 9]$); the resulting ranges are dispatched to HBase as `Scan` commands.

d) *3D spatial queries with ZFilter*: When an altitude band $[q_z^{\min}, q_z^{\max}]$ is specified, the above 2D scan ranges remain unchanged. Instead, AeroMesa augments the scan with a server-side HBase filter on the `meta:zmin/zmax` cells (Section IV-E), pruning non-qualifying segments at the region server before payload transfer.

C. Spatio-Temporal Query

A spatio-temporal query $(Q_R, [t_{qs}, t_{qe}])$ is processed by the HTSI index of Section IV-F. When an altitude band is specified, its span satisfies $\Delta q_z \leq 64$ m, and both bounds lie inside the nominal domain $[0, 1024)$ m, AeroMesa selects the finest HTSI level k^* with $\Delta q_z \leq w_{k^*}/2$ and resolves the single fully-covering slot h^* (Eq. (10)); otherwise, the query falls back to the height-agnostic base TSI with altitude filtering delegated to the ZFilter layer.

The resulting rowkey range

$$[BinNum \parallel h^* \parallel LS_{\min}, BinNum \parallel h^* \parallel LS_{\max}] \quad (16)$$

is contiguous on a single HBase region, where LS_{\min} and LS_{\max} are the lower and upper bounds of the concatenated field $LS = SI \parallel SegTimeID$.

When the query time window spans multiple days, one contiguous scan per $BinNum$ is issued independently; the resulting candidate sets are merged before downstream ZFilter and payload evaluation.

VI. EXPERIMENTAL EVALUATION

This section evaluates AeroMesa across four dimensions: temporal range queries, 2D/3D spatial range queries, 4D spatio-temporal queries, and scalability.

1) *Datasets*: We evaluate the efficiency and scalability of Aeromesa using three datasets:

- **TDrive**: This dataset contains the GPS trajectories of 10,357 taxis in Beijing from February 2 to February 8, 2008. It includes approximately 15 million GPS points, with a total trajectory distance of 9 million kilometers.
- **Synthetic-TDrive**: For scalability evaluation, we first sample 1,000 trajectories from T-Drive as a $1 \times$ seed set, then generate larger datasets via random spatial translation and temporal shifting. This produces data scales up to $200 \times$ (200,000 trajectories).
- **UAV Synthetic Dataset**. We generated 90,000 UAV mission trajectories over a $10,000 \times 10,000$ m area in Xuhui District, Shanghai, using a physics-fidelity simulation pipeline combining ROS [37], Gazebo [38], and PX4 [39], with the Gazebo world configured to include realistic wind fields and weather variability. Trajectories are planned via a grid-based A* algorithm over an environment map derived from real OpenStreetMap road networks, building footprints, and no-fly zone constraints, ensuring that generated paths respect realistic urban airspace geometry. The simulated airspace spans 0–120 m AGL following the FAA low-altitude operational boundary [35], with ten mission types distributed across dedicated altitude bands under the layered airspace

stratification principle [36]. Each trajectory sequences four primitive maneuvers—cruise, climb/descent, vertical climb, and hover—to replicate realistic flight dynamics. To ensure operational generality across the statutory 1000 m low-altitude economy airspace ceiling, the system boundary is provisioned up to 1024 m, while our evaluation dataset is bounded within the regulatory 0–120 m AGL flight zone for lightweight UAVs. This spatial gap does not artificially inflate evaluation efficiency: all 3D/4D query workloads are executed strictly within the active 0–120 m dense cluster rather than vertical empty space. Furthermore, empty slots above 120 m generate zero key or metadata footprint under our storage layout.

2) *Settings*: Each benchmark reports the average over 100 queries with distinct, randomly-shifted spatio-temporal windows. All experiments are repeated over 10 independent trials, and the query bounds are freshly re-generated per run. Crucially, the relative performance gains of AeroMesa and the optimization trends in our ablation studies remain invariant under these varying conditions. All baselines are evaluated with identical concurrency and workflow configurations to ensure fairness. We evaluated Aeromesa on hardware with 16-core CPU, 256GB RAM, and 16TB disk. The software stack includes Hadoop 3.3.4, HBase 2.5.8, and Redis 6.0.16. To align with the design assumptions of TMan and MCTM, AeroMesa’s primary table and secondary index tables are deployed on the same HBase instance, while the in-memory shape-code cache is maintained in Redis.

3) *Baselines*: We compare AeroMesa against four representative systems. **TMan**, the current state of the art for 2D spatial range queries, serves as our primary spatial-index baseline; since its code is not publicly available, we re-implemented it faithfully, and the observed gains are consistent with those reported in the paper. **MCTM**, which achieves state-of-the-art performance on temporal and spatio-temporal queries, is included using the authors’ official source code. **GeoMesa** is used as a general-purpose open-source baseline. Finally, we include curve-only baselines—XZ2 for 2D queries and XZ3/WXZ3 for 3D and TXZ3/TWXZ3 for 4D queries—to isolate the benefit of higher-level index engineering over raw space-filling curves.

A. Temporal Range Query

Figure 9 compares TI^+ and TI across query durations from 300 s to 43,200 s on our UAV dataset.

TI^+ consistently outperforms TI across all durations. For short windows (300–900 s), TI^+ lowers average query time from 12.07–13.48 ms/query to 9.56–10.62 ms/query (20.8%–21.2% reduction), while candidate segments decrease by 36.4%–51.3%. At 3600 s, TI^+ still achieves an 8.0% average-time reduction (16.93 to 15.58 ms/query) and a 20.5% candidate reduction. For long windows (14,400–43,200 s), the average-time gain remains 5.5%–5.9% (34.38 to 32.34 ms/query and 130.56 to 123.42 ms/query), with 2.3%–6.5% fewer candidates.

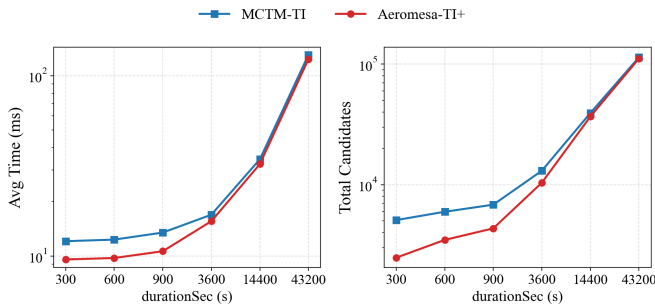


Fig. 9: TI vs. TI⁺ on temporal range queries: average query time (left) and candidate segments (right).

B. 2D Spatial Range Query

We next evaluate 2D spatial query latency on both T-Drive and UAV datasets. Query windows are grouped by side length: *small* (300 × 300 m), *medium* (500 × 500 m), *large* (1000 × 1000 m), *xlarge* (2000 × 2000 m), and *xxlarge* (5000 × 5000 m).

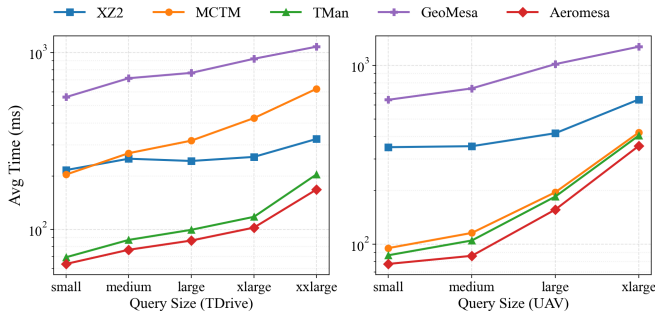


Fig. 10: 2D spatial query latency (left: T-Drive, right: UAV).

Figure 10 shows AeroMesa achieves the lowest latency on both datasets. On T-Drive it reduces latency by 8.3%–17.9% over TMan, 68.8%–76.0% over MCTM, 48.2%–70.6% over XZ2, and 84.4%–89.3% over GeoMesa; results on UAV are consistent (10.6%–17.9% over TMan; 72.1%–88.4% over GeoMesa).

1) *Ablation: Independent Gains of Hilbert-BFS and WAJ*: We isolate each component by comparing: *TMan* (XZ2+Jaccard), *XZ2+WAJ*, *Hilbert-BFS+Jaccard*, and *AeroMesa* (Hilbert-BFS+WAJ).

Figure 11 shows both components contribute independently: WAJ alone reduces latency by 2.5%–5.9% (T-Drive) and 5.5%–8.1% (UAV); Hilbert-BFS alone by 2.2%–13.2% and 4.1%–15.5%. Combined, AeroMesa improves 8.3%–17.9% over TMan (T-Drive) and 10.6%–17.9% (UAV), with WAJ adding a further 1.7%–6.3% and 2.8%–11.8% on top of Hilbert-BFS alone.

C. 3D Spatial Range Query

We use default *XZ3* (altitude $\in [0, 1000]$ m) as the primary curve baseline, with query footprints of 1000 × 1000 m and altitude-range classes {10, 25, 50, 100, 250} m. *WXZ3* is a novel asymmetric variant we propose that replaces *XZ3*'s

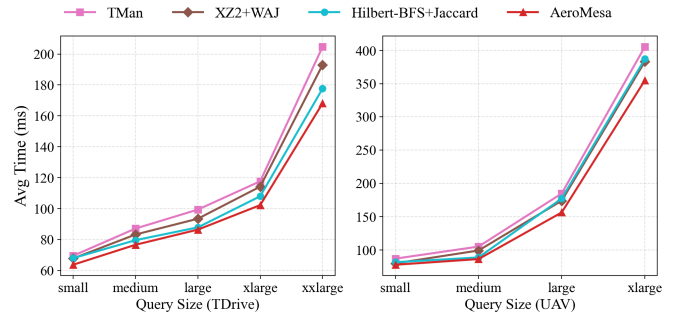


Fig. 11: Ablation on 2D spatial queries (left: T-Drive, right: UAV).

isotropic 2×2×2 subdivision (1/1/1 bits per $x/y/z$) with 4×4×2 (2/2/1 bits) to form a standard 32-ary tree. For example, after 9 levels, its 18-bit horizontal ($\Delta_{xy} \approx 152$ m) and 9-bit vertical ($\Delta_z = 2$ m) resolutions tightly map a 1000×1000×10 m query to a compact 6×6×5 cell block, making the index granularity closely fit our segments and query box. *WXZ3* thus serves as a highly-optimized and competitive joint-encoding baseline that partially mitigates the aspect-ratio mismatch through asymmetric bit allocation; however, it remains fundamentally constrained by the isotropic SFC framework and is therefore treated as a baseline rather than a contribution of this work.

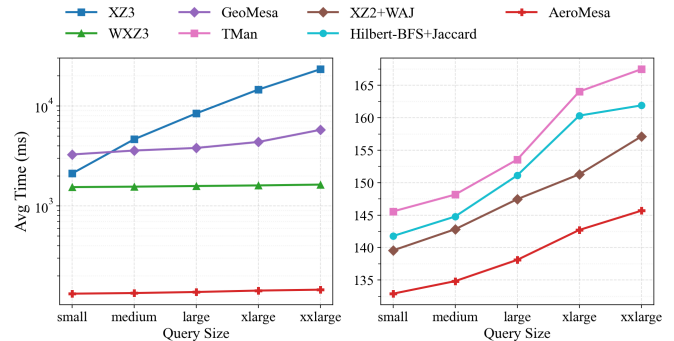


Fig. 12: 3D spatial query latency (left: main baseline comparison; right: ablation of Hilbert-BFS and WAJ).

Figure 12 (left) shows AeroMesa remains nearly flat at 132.9–145.7 ms (1.10×), while *XZ3* escalates 11.03× (to 23293.2 ms). *WXZ3* stays much flatter (1.06×, 1543.9–1635.9 ms) but is still consistently slower than AeroMesa. AeroMesa reduces latency by 93.7%–99.4% over *XZ3*, 91.1%–91.4% over *WXZ3*, and 95.9%–97.5% over *GeoMesa*. The right panel confirms the ablation trend: WAJ contributes 3.6%–7.8%, Hilbert-BFS 1.6%–3.3%, and combined they yield 8.7%–13.0% improvement over the TMan-style baseline, with WAJ adding 6.3%–11.0% on top of Hilbert-BFS.

D. Spatio-Temporal Query (4D)

We evaluate 4D queries in two complementary settings. In all queries, the query footprint is fixed to 1000 × 1000 m. First, we fix the temporal window at 30000 s

and vary altitude range over $\{5, 15, 30, 60, 120, 240\}$ m. Second, we fix height range at 15 m and vary duration over $\{3600, 7200, 15000, 30000, 60000, 180000\}$ s.

TXZ3 uses default XZ3 as the spatial index key, while TWXZ3 uses weighted XZ3; base TSI uses 2D Hilbert-BFS without height slots; AeroMesa-HTSI adds a HeightSlot prefix for altitude pre-pruning.

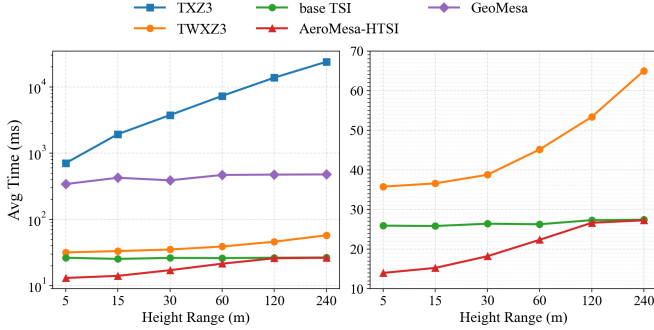


Fig. 13: 4D spatio-temporal query with fixed time (left: main comparison; right: TWXZ3, base TSI, and HTSI).

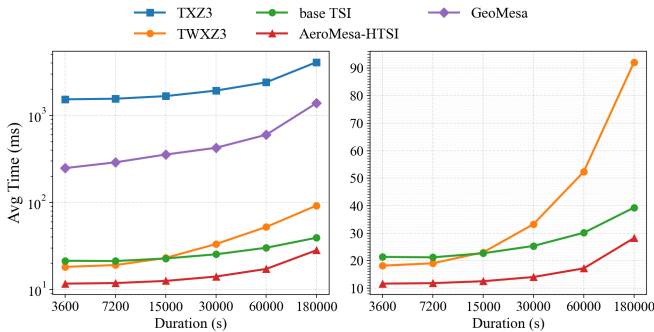


Fig. 14: 4D spatio-temporal query with fixed height (left: main comparison; right: TWXZ3, base TSI, and HTSI).

Figure 13 shows that, under a fixed 30000 s window, HTSI grows from 13.07 ms to 26.37 ms as altitude range increases, versus 25.37–26.63 ms for base TSI, yielding 1.0%–50.4% lower latency. Relative to TXZ3, TWXZ3, and GeoMesa, HTSI reduces latency by 98.1%–99.9%, 43.8%–58.9%, and 94.5%–96.7%, respectively. The gain over base TSI comes from HeightSlot pruning: candidate segments drop from 1603.64 to 418.54–1232.65 while the merged scan range count remains unchanged for both variants. The larger gap against TXZ3 is due to joint-encoding fragmentation: average merged ranges rise to 15,736–554,328 for TXZ3, compared with 105.65–491.84 for TWXZ3 and 57.44 for base TSI/HTSI.

Figure 14 shows the same pattern when height is fixed at 15 m and duration increases. HTSI rises from 11.67 ms to 28.24 ms, compared with 21.23 ms to 39.31 ms for base TSI, preserving a 28.1%–45.4% latency reduction across all durations. Against TXZ3, TWXZ3, and GeoMesa, HTSI remains 99.2%–99.3%, 35.9%–69.4%, and 95.3%–97.9%

faster, respectively. Again, the HTSI–base TSI gap comes from lower candidate counts (386.76–1470.66 vs. 1197.63–3825.66), while both variants keep the same merged scan ranges (43.9–128.95); in contrast, TXZ3 still incurs much heavier fragmentation, with average merged ranges reaching 35,665–104,875, while TWXZ3 reduces this to 98.56–290.08.

E. Scalability

We evaluate scalability on Synthetic-TDrive with data scales from $1\times$ to $200\times$, using 2D query workload (500×500 m).

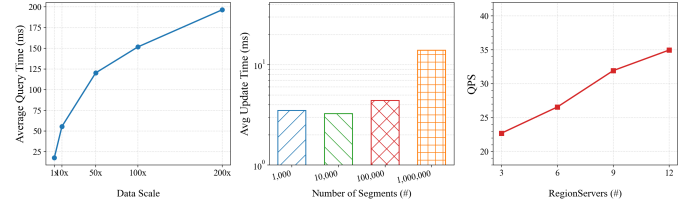


Fig. 15: Scalability of AeroMesa on Synthetic-TDrive

Figure 15 (left) shows query latency grows from 17.82 ms ($1\times$) to 196.47 ms ($200\times$)—an $11.03\times$ increase for $200\times$ data growth, confirming sub-linear read scalability.

The middle panel reports the amortized write cost of batch-inserting 4,000 segments into a store of varying size. The per-segment update time stays stable at 3.26–4.40 ms for up to 100,000 existing segments, and rises moderately to 13.95 ms at 1,000,000 segments—a $4.3\times$ increase for a $1000\times$ growth in store size. This sub-linear growth is attributed to the main+delta LSM design (Section IV-C3), which amortizes WAJ re-encoding across background compaction batches.

The right panel reports distributed query throughput under the same intensive workload comprising 1,000 simultaneous queries (each with a 500×500 meter 2D spatial window) on the T-Drive dataset. As RegionServer instances increase from 3 to 12, throughput rises from 22.7 to 35.0 QPS, a 54.1% improvement. The gain is sub-linear, attributed to resource contention and RPC overhead under high concurrency.

VII. CONCLUSION

This paper presents AeroMesa, an efficient multi-dimensional spatio-temporal trajectory management system built on Apache HBase and Redis, targeting the emerging low-altitude UAV trajectory workload. We identify row-key interval fragmentation as the core bottleneck of naive joint spatial encodings and address it through a decoupled architecture: the Spatial Index (SI) encodes only horizontal coordinates via Hilbert-BFS, with altitude filtering pushed down to a server-side ZFilter for 3D queries. For 4D spatio-temporal queries, the HTSI secondary index organizes segments by multi-granularity altitude slots, directly pruning irrelevant altitude bands without decoding any point sequence. Interesting future work includes: 1) scaling AEROMESA to larger distributed deployments by devising workload-aware partitioning strategies to mitigate high-concurrency RPC overhead and balance storage locality; and 2) extending AEROMESA to support efficient k -nearest-neighbor and trajectory similarity queries.

REFERENCES

- [1] S. Ruan, C. Long, J. Bao, C. Li, Z. Yu, R. Li, and Y. Zheng, "Learning to generate maps from trajectories," in *Proceedings of the AAAI Conference on Artificial Intelligence*, vol. 34, no. 1, 2020, pp. 890–897.
- [2] R. Li, H. He, R. Wang, S. Ruan, T. He, J. Bao, J. Zhang, L. Hong, and Y. Zheng, "Trajmesa: A distributed nosql-based trajectory data management system," *IEEE Transactions on Knowledge and Data Engineering*, vol. 35, no. 1, pp. 1013–1027, 2021.
- [3] H. Lan, J. Xie, Z. Bao, F. Li, W. Tian, F. Wang, S. Wang, and A. Zhang, "Vre: a versatile, robust, and economical trajectory data system," *Proceedings of the VLDB Endowment*, vol. 15, no. 12, pp. 3398–3410, 2022.
- [4] H. He, Z. Xu, R. Li, J. Bao, T. Li, and Y. Zheng, "Tman: a high-performance trajectory data management system based on key-value stores," in *2024 IEEE 40th International Conference on Data Engineering (ICDE)*. IEEE, 2024, pp. 4951–4964.
- [5] P. Cudre-Mauroux, E. Wu, and S. Madden, "Trajstore: An adaptive storage system for very large trajectory data sets," in *2010 IEEE 26th International Conference on Data Engineering (ICDE 2010)*. IEEE, 2010, pp. 109–120.
- [6] S. Wang, Z. Bao, J. S. Culpepper, Z. Xie, Q. Liu, and X. Qin, "Torch: A search engine for trajectory data," in *The 41st international ACM SIGIR conference on research & development in information retrieval*, 2018, pp. 535–544.
- [7] L. Alarabi, M. F. Mokbel, and M. Musleh, "St-hadoop: A mapreduce framework for spatio-temporal data," *GeoInformatica*, vol. 22, no. 4, pp. 785–813, 2018.
- [8] L. Alarabi, "Summit: a scalable system for massive trajectory data management," in *Proceedings of the 26th ACM SIGSPATIAL International Conference on Advances in Geographic Information Systems*, 2018, pp. 612–613.
- [9] X. Ding, L. Chen, Y. Gao, C. S. Jensen, and H. Bao, "Ultraman: A unified platform for big trajectory data management and analytics," *Proceedings of the VLDB Endowment*, vol. 11, no. 7, pp. 787–799, 2018.
- [10] Z. Shang, G. Li, and Z. Bao, "Dita: Distributed in-memory trajectory analytics," in *Proceedings of the 2018 International Conference on Management of Data*, 2018, pp. 725–740.
- [11] Z. Zhang, C. Jin, J. Mao, X. Yang, and A. Zhou, "Trajspark: A scalable and efficient in-memory management system for big trajectory data," in *Asia-Pacific Web (APWeb) and Web-Age Information Management (WAIM) Joint Conference on Web and Big Data*. Springer, 2017, pp. 11–26.
- [12] Z. Fang, L. Chen, Y. Gao, L. Pan, and C. S. Jensen, "Dragon: a hybrid and efficient big trajectory management system for offline and online analytics," *VLDB Journal International Journal on Very Large Data Bases*, vol. 30, no. 2, p. 287, 2021.
- [13] E. Zimányi, M. Sakr, and A. Lesuisse, "Mobilitydb: A mobility database based on postgresql and postgis," *ACM Transactions on Database Systems (TODS)*, vol. 45, no. 4, pp. 1–42, 2020.
- [14] D. Xie, F. Li, B. Yao, G. Li, L. Zhou, and M. Guo, "Simba: Efficient in-memory spatial analytics," in *Proceedings of the 2016 international conference on management of data*, 2016, pp. 1071–1085.
- [15] J. Yu, J. Wu, and M. Sarwat, "Geospark: A cluster computing framework for processing large-scale spatial data," in *Proceedings of the 23rd SIGSPATIAL international conference on advances in geographic information systems*, 2015, pp. 1–4.
- [16] J. N. Hughes, A. Annex, C. N. Eichelberger, A. Fox, A. Hulbert, and M. Ronquest, "Geomesa: a distributed architecture for spatio-temporal fusion," in *Geospatial informatics, fusion, and motion video analytics V*, vol. 9473. SPIE, 2015, pp. 128–140.
- [17] Y. Tao, H. Chen, Z. Lin, J. Xu, X. Gao, J. Wang, Y. Jiao, and Y. Xu, "Mctm: Multi-chord distributed system for efficient trajectory data management in mobile edge computing," in *International Conference on Database Systems for Advanced Applications*. Springer, 2025, pp. 673–682.
- [18] J. Qin, L. Ma, and J. Niu, "Thbase: A coprocessor-based scheme for big trajectory data management," *Future Internet*, vol. 11, no. 1, p. 10, 2019.
- [19] A. Guttman, "R-trees: A dynamic index structure for spatial searching," in *Proceedings of the 1984 ACM SIGMOD international conference on Management of data*, 1984, pp. 47–57.
- [20] N. Beckmann, H.-P. Kriegel, R. Schneider, and B. Seeger, "The r*-tree: An efficient and robust access method for points and rectangles," in *Proceedings of the 1990 ACM SIGMOD international conference on Management of data*, 1990, pp. 322–331.
- [21] Y. Tao, D. Papadias, and J. Sun, "The tpr*-tree: An optimized spatio-temporal access method for predictive queries," in *Proceedings 2003 VLDB conference*. Elsevier, 2003, pp. 790–801.
- [22] J. Yu and M. Sarwat, "Two birds, one stone: A fast, yet lightweight, indexing scheme for modern database systems," *Proc. VLDB Endow.*, vol. 10, no. 4, pp. 385–396, 2016.
- [23] I. Kamel and C. Faloutsos, "Hilbert r-tree: An improved r-tree using fractals," 1993.
- [24] L. Wang, Y. Zheng, X. Xie, and W.-Y. Ma, "A flexible spatio-temporal indexing scheme for large-scale gps track retrieval," in *The Ninth International Conference on Mobile Data Management (mdm 2008)*. IEEE, 2008, pp. 1–8.
- [25] C. Böxhm, G. Klump, and H.-P. Kriegel, "Xz-ordering: A space-filling curve for objects with spatial extension," in *International Symposium on Spatial Databases*. Springer, 1999, pp. 75–90.
- [26] R. Li, H. He, R. Wang, Y. Huang, J. Liu, S. Ruan, T. He, J. Bao, and Y. Zheng, "Just: Jd urban spatio-temporal data engine," in *2020 IEEE 36th International Conference on Data Engineering (ICDE)*. IEEE, 2020, pp. 1558–1569.
- [27] H. He, R. Li, S. Ruan, T. He, J. Bao, T. Li, and Y. Zheng, "Trass: Efficient trajectory similarity search based on key-value data stores," in *2022 IEEE 38th International conference on data engineering (ICDE)*. IEEE, 2022, pp. 2306–2318.
- [28] B. Moon, H. V. Jagadish, C. Faloutsos, and J. H. Saltz, "Analysis of the clustering properties of the hilbert space-filling curve," *IEEE Transactions on knowledge and data engineering*, vol. 13, no. 1, pp. 124–141, 2001.
- [29] H. Liu, J. Yan, J. Wang, B. Chen, M. Chen, and X. Huang, "Hgst: A hilbert-geosot spatio-temporal meshing and coding method for efficient spatio-temporal range query on massive trajectory data," *ISPRS International Journal of Geo-Information*, vol. 12, no. 3, p. 113, 2023.
- [30] D. Pfoser, C. S. Jensen, Y. Theodoridis *et al.*, "Novel approaches to the indexing of moving object trajectories," in *VLDB*, vol. 2000, 2000, pp. 395–406.
- [31] Q. Zhu, J. Gong, and Y. Zhang, "An efficient 3d r-tree spatial index method for virtual geographic environments," *ISPRS Journal of Photogrammetry and Remote Sensing*, vol. 62, no. 3, pp. 217–224, 2007.
- [32] H. He, R. Li, J. Bao, T. Li, and Y. Zheng, "Just-traj: A distributed and holistic trajectory data management system," in *Proceedings of the 29th International Conference on Advances in Geographic Information Systems*, 2021, pp. 403–406.
- [33] J. Yuan, Y. Zheng, C. Zhang, W. Xie, X. Xie, G. Sun, and Y. Huang, "T-drive: driving directions based on taxi trajectories," in *Proceedings of the 18th SIGSPATIAL International conference on advances in geographic information systems*, 2010, pp. 99–108.
- [34] C. Luo, "The civil unmanned aerial vehicle (uav) law of china: A comparative study of the mainland, hong kong, and macao," in *The Regulation of Automated and Autonomous Transport*. Springer, 2023, pp. 71–103.
- [35] P. H. Kopardekar, "Unmanned aircraft system (uas) traffic management (utm): Enabling civilian low-altitude airspace and unmanned aerial system operations," *Unmanned Aircraft System (UAS) Traffic Management (UTM): Enabling Civilian Low-Altitude Airspace and Unmanned Aerial System Operations by Kopardekar*, p. 08685, 2016.
- [36] A. Bauranov and J. Rakas, "Designing airspace for urban air mobility: A review of concepts and approaches," *Progress in Aerospace Sciences*, vol. 125, p. 100726, 2021.
- [37] M. Quigley, K. Conley, B. Gerkey, J. Faust, T. Foote, J. Leibs, R. Wheeler, A. Y. Ng *et al.*, "Ros: an open-source robot operating system," in *ICRA workshop on open source software*, vol. 3, no. 3.2. Kobe, 2009, p. 5.
- [38] N. Koenig and A. Howard, "Design and use paradigms for gazebo, an open-source multi-robot simulator," in *2004 IEEE/RSJ international conference on intelligent robots and systems (IROS)(IEEE Cat. No. 04CH37566)*, vol. 3. Ieee, 2004, pp. 2149–2154.
- [39] L. Meier, D. Honegger, and M. Pollefeys, "Px4: A node-based multithreaded open source robotics framework for deeply embedded platforms," in *2015 IEEE international conference on robotics and automation (ICRA)*. IEEE, 2015, pp. 6235–6240.